

**UNCLASSIFIED**

ERIM-119400-2-F

F44620-76-C-0047

NL

1 OF 1  
AD  
A054904

100

END  
DATE  
FILMED  
7-78

DDC

FOR FURTHER TRAN

2 (2)

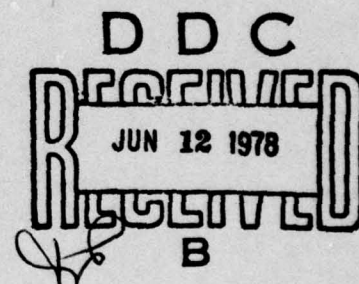
AD A054904  
119400-2-F

Final Scientific Report  
**OPTICAL PROCESSORS  
USING HOLOGRAPHIC OPTICAL ELEMENTS**

JAMES R. FIENUP  
Radar and Optics Division

MAY 1978

Approved for Public Release;  
Distribution Unlimited.



Directorate of Electronics & Solid State Sciences  
AFOSR/NE, Bolling AFB  
Washington, DC 20332

ADJ NO.  
DDC FILE COPY

**ENVIRONMENTAL  
RESEARCH INSTITUTE OF MICHIGAN**  
FORMERLY WILLOW RUN LABORATORIES, THE UNIVERSITY OF MICHIGAN  
BOX 8618 • ANN ARBOR • MICHIGAN 48107

**DISTRIBUTION STATEMENT A**

Approved for public release;  
Distribution Unlimited

**AIR FORCE OFFICE OF SCIENTIFIC RESEARCH (AFSC)**

**NOTICE OF TRANSMITTAL TO DDC**

This technical report has been reviewed and is  
approved for public release IAW AFR 190-12 (7b).  
Distribution is unlimited.

**A. D. BLOSE**

Technical Information Officer



UNCLASSIFIED

SECURITY CLASSIFICATION OF THIS PAGE (When Data Entered)

19 REPORT DOCUMENTATION PAGE		READ INSTRUCTIONS BEFORE COMPLETING FORM
1. REPORT NUMBER AFOSR/TR-78-0979	2. GOVT ACCESSION NO.	3. RECIPIENT'S CATALOG NUMBER
4. TITLE (and Subtitle) OPTICAL PROCESSORS USING HOLOGRAPHIC OPTICAL ELEMENTS	5. TYPE OF REPORT & PERIOD COVERED Final Scientific Report 1 Nov 75-31 Dec 77	6. PERFORMING ORG. REPORT NUMBER 119400-2-F
7. AUTHOR(s) James R./Fienup	8. CONTRACT OR GRANT NUMBER(s) F44620-76-C-0047	
9. PERFORMING ORGANIZATION NAME AND ADDRESS Environmental Research Institute of Michigan P.O. Box 8618 Ann Arbor, MI 48107	10. PROGRAM ELEMENT, PROJECT, TASK AREA & WORK UNIT NUMBERS 61102F/2305/B2	
11. CONTROLLING OFFICE NAME AND ADDRESS Directorate of Electronics & Solid State Sciences AFOSR/NE, Building 410 Bolling AFB, Washington, DC 20332	12. REPORT DATE May 1978	13. NUMBER OF PAGES 61
14. MONITORING AGENCY NAME AND ADDRESS (if different from Controlling Office)	15. SECURITY CLASS. (of this report) Unclassified	15a. DECLASSIFICATION/DOWNGRADING SCHEDULE
16. DISTRIBUTION STATEMENT (of this Report) Approved for public release; distribution unlimited.		
17. DISTRIBUTION STATEMENT (of the abstract entered in Block 20, if different from Report)		
18. SUPPLEMENTARY NOTES		
19. KEY WORDS (Continue on reverse side if necessary and identify by block number) Optical processing      Matched filter Holographic optics      Computer design Holography      Ray tracing		
20. ABSTRACT (Continue on reverse side if necessary and identify by block number) This report describes an investigation of holographic optical elements for use in optical data processors. Thin, lightweight, potentially inexpensive, and allowing compact folded light paths, holographic optics offers significant advantages in applications such as optical processors for terminal guidance. Holographic lenses for a matched-filter optical processor and a Fourier spectrum processor were designed and analyzed. Holographic lenses		

DD FORM 1473 EDITION OF 1 NOV 65 IS OBSOLETE

UNCLASSIFIED

SECURITY CLASSIFICATION OF THIS PAGE (When Data Entered)

407 903

mt



UNCLASSIFIED

SECURITY CLASSIFICATION OF THIS PAGE(When Data Entered)

20. Abstract (continued)

were fabricated and assembled into optical processors; and the performance of the processors was measured and compared to the analysis. Both the analytical and the experimental results of this research suggest that holographic optics can perform well as the Fourier transforming lenses in optical processors, making them an attractive alternative to conventional optics for those optical processing applications that can benefit from the unique properties of holographic optics. A useful quality criterion that was developed for analyzing matched filter optical processors is the standard deviation phase error criterion.

ACCESSION NO.	
NTIS	Write Section <input checked="" type="checkbox"/>
DDC	DDC Section <input type="checkbox"/>
UNANNOUNCED	<input type="checkbox"/>
JUSTIFICATION	
BY	
DISTRIBUTION/AVAILABILITY CODES	
Dist.	AVAIL. ONLY OR SPECIAL
A	

UNCLASSIFIED

## FOREWORD

This report was prepared by the Radar and Optics Division of the Environmental Research Institute of Michigan. The work was sponsored by the Air Force Office of Scientific Research under Contract No. F44620-76-C-0047.

This final report covers work performed between 1 November 1975 and 31 December 1977. The contract monitor is Captain John A. Neff, Directorate of Electronics and Solid State Sciences, AFOSR/NE, Building 410, Bolling Air Force Base, Washington, D.C. 20332. The principal investigator is James R. Fienup. Major contributors to the effort are James R. Fienup, Carl D. Leonard, David B. Franczak, Carl C. Aleksoff, Mohamed Hidayet, and Willis S. Colburn.

Preceding Page BLANK - NOT FILMED



FORMERLY WILLOW RUN LABORATORIES, THE UNIVERSITY OF MICHIGAN

## CONTENTS

Foreword.....	3
List of Figures.....	6
Real-Time Optical Processor.....	10
SAR Data Processor.....	15
Conclusions.....	15
Appendix A: Holographic Optics for a Matched- Filter Optical Processor.....	A-1



## FIGURES

1. Matched-filter optical processor using holographic optical elements.....	11
2. Real-time matched-filter optical processor using holographic optics.....	12
3. Real-time matched-filter optical processor using holographic optical elements.....	13
4. Scan through output of real-time matched filter optical processor.....	14

## Appendix A

1. Configurations of optical processors using (a) conventional optics and (b) holographic optics.....	A-36
2. Computer simulation of matched filter output with aberrations...	A-37
3. Recording geometry for 10° offset Fourier transforming holographic lens.....	A-38
4. Performance of 100 mm focal length Fourier transforming holographic lens: the linear space-bandwidth product of the total image vs. the linear space-bandwidth product of the area of interest, for various values of the width ( $D_s$ ) of the area of interest and of the maximum spatial frequency of the image.....	A-39
5. Translation $x_o$ of the input resulting in $\sigma_1 = \lambda/8$ , vs. focal length ( $F$ ), for various widths ( $D_s$ ) of the image of interest....	A-40
6. Performance of holographic lens for Fourier spectrum analysis, assuming $\sigma \leq \lambda/8$ at 40 cyc/mm.....	A-41
7. Diffraction efficiency vs. angle of illumination for holographic lenses A and B.....	A-42
8. Interferometer for testing holographic lenses.....	A-43
9. Interferograms of holographic lenses A and B.....	A-44
10. Input image for correlation experiments.....	A-45
11. Scan through peak of output, $x_o = 4$ mm.....	A-46

## FIGURES (Continued)

- 12. Intensity of output peak vs.  $x_o$  .....A-47
- 13. Scan through peak of output,  $x_o = 21$  mm.....A-48
- 14. Imaging system using a holographic lens.....A-49
- 15. Output image.....A-50



Final Scientific Report  
OPTICAL PROCESSORS USING HOLOGRAPHIC OPTICAL ELEMENTS

This report describes a two-phase effort to investigate holographic optical elements for use in optical processors. In the first phase, holographic optics for a matched filter optical processor and holographic optics for a Fourier transform optical processor were designed and analyzed. In the second phase, holographic optics were fabricated, tested, and assembled into optical processors; optical processing experiments were undertaken, and the performance of the processors was compared with that predicted by the analysis. The results of this research suggest that holographic lenses are an attractive alternative to conventional optics for those optical processing applications that benefit from the unique advantages of holographic optics. These advantages include their light weight, compact design, low cost, and ability to perform multiple functions.

Major results of this research are described in Appendix A of this report, which is prepared in the form of a paper entitled, "Holographic Optics for a Matched-Filter Optical Processor," [1] which is being submitted for publication. Another publication resulting from this work is Ref. 2.

Important topics not covered in Appendix A comprise the remainder of the body of this report. The topics include the implementation of a real-time optical processor and a synthetic aperture radar processor.

1. J.R. Fienup and C.D. Leonard, "Holographic Optics for a Matched-Filter Optical Processor," submitted for publication to Applied Optics.
2. J.R. Fienup, W.S. Colburn, B.J. Chang, and C.D. Leonard, "Compact Real-Time Matched-Filter Optical Processor," Proc. SPIE 118, Optical Signal and Image Processing, p. 21 (August 1977).



## REAL-TIME OPTICAL PROCESSOR

The optical processor used for the experiments described in Appendix A is shown in Figure 1 (a schematic diagram of which is shown in Figure 1(b) of Appendix A). A collimated beam illuminates the input transparency (S), the Fourier transform of which is brought to focus at the matched filter plane (F) by the reflective holographic lens ( $H_1$ ). The wavefront emerging from the filter is brought to focus at the output plane (OD) by a second reflective holographic lens ( $H_2$ ). The collimating lens  $L_r$  provides a plane wave reference beam for recording the matched filter.

In addition to those described in Appendix A, correlation experiments were performed with a photoconductor-thermoplastic device as the input in order to demonstrate the concept of a lightweight and compact real-time matched-filter optical processor. The photoconductor-thermoplastic device was developed in a parallel effort sponsored by the Air Force Office of Scientific Research under Contract No. F44620-76-C-0053. The experimental setup, including the real-time input, is shown in the diagram of Figure 2 and the photograph in Figure 3. A transparency (A) is illuminated with incoherent light and imaged via a beamsplitter (B) onto the photoconductor-thermoplastic device (S) which is in the input plane to the optical processor. A grating (G) is sandwiched with the transparency (A) in order to provide a spatial frequency offset as required by the band-pass response of the photoconductor-thermoplastic device. The photoconductor-thermoplastic device acts as an incoherent-to-coherent transducer enabling new data to be entered in real-time at the input of the coherent optical processor. Figure 4 shows a scan through correlation output achieved with the real-time processor. A signal-to-noise ratio exceeding 30 dB and a 3 dB spot width of 47  $\mu\text{m}$

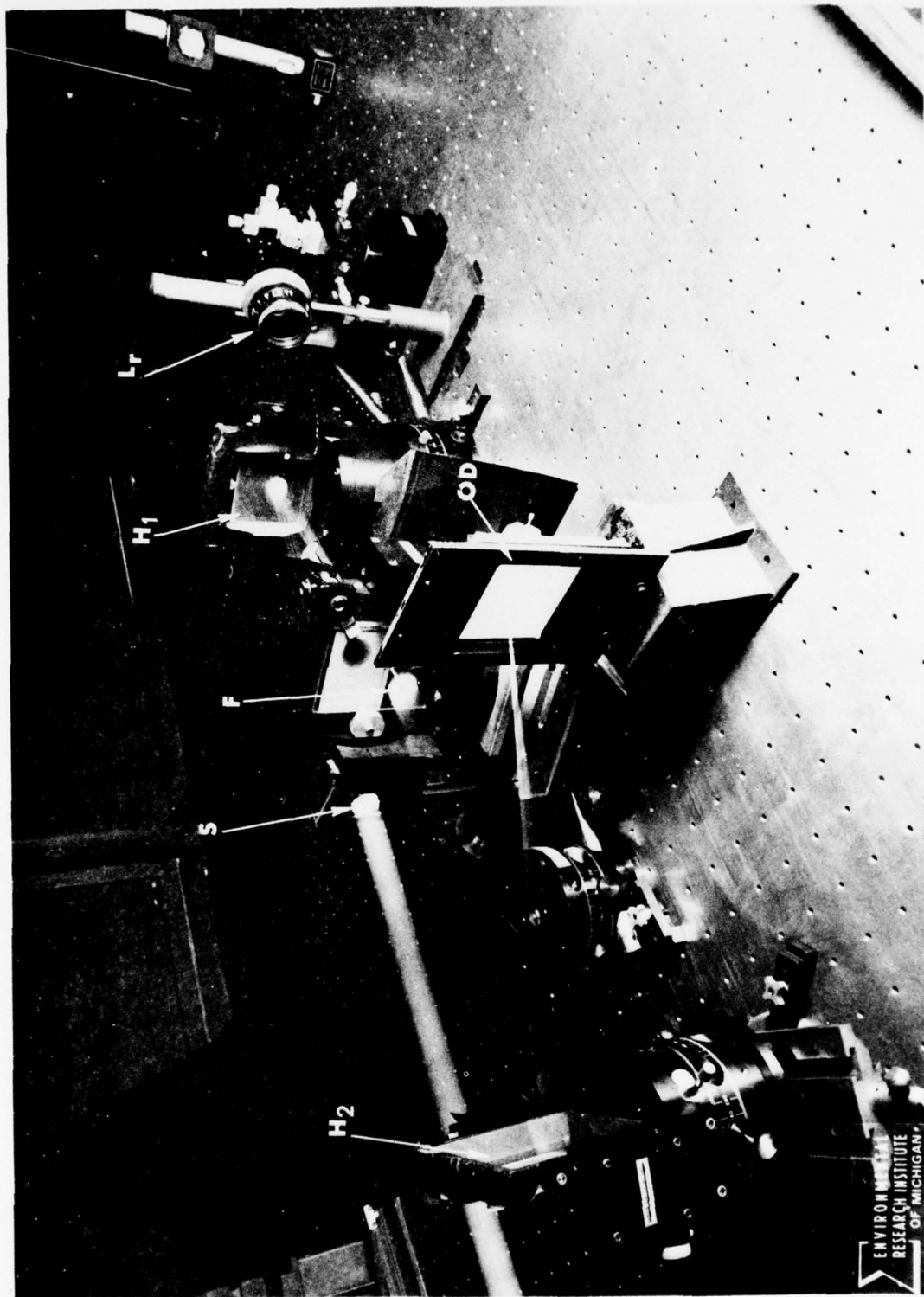
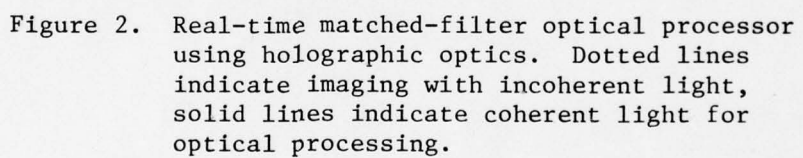


Figure 1. Matched-filter optical processor using holographic optical elements.





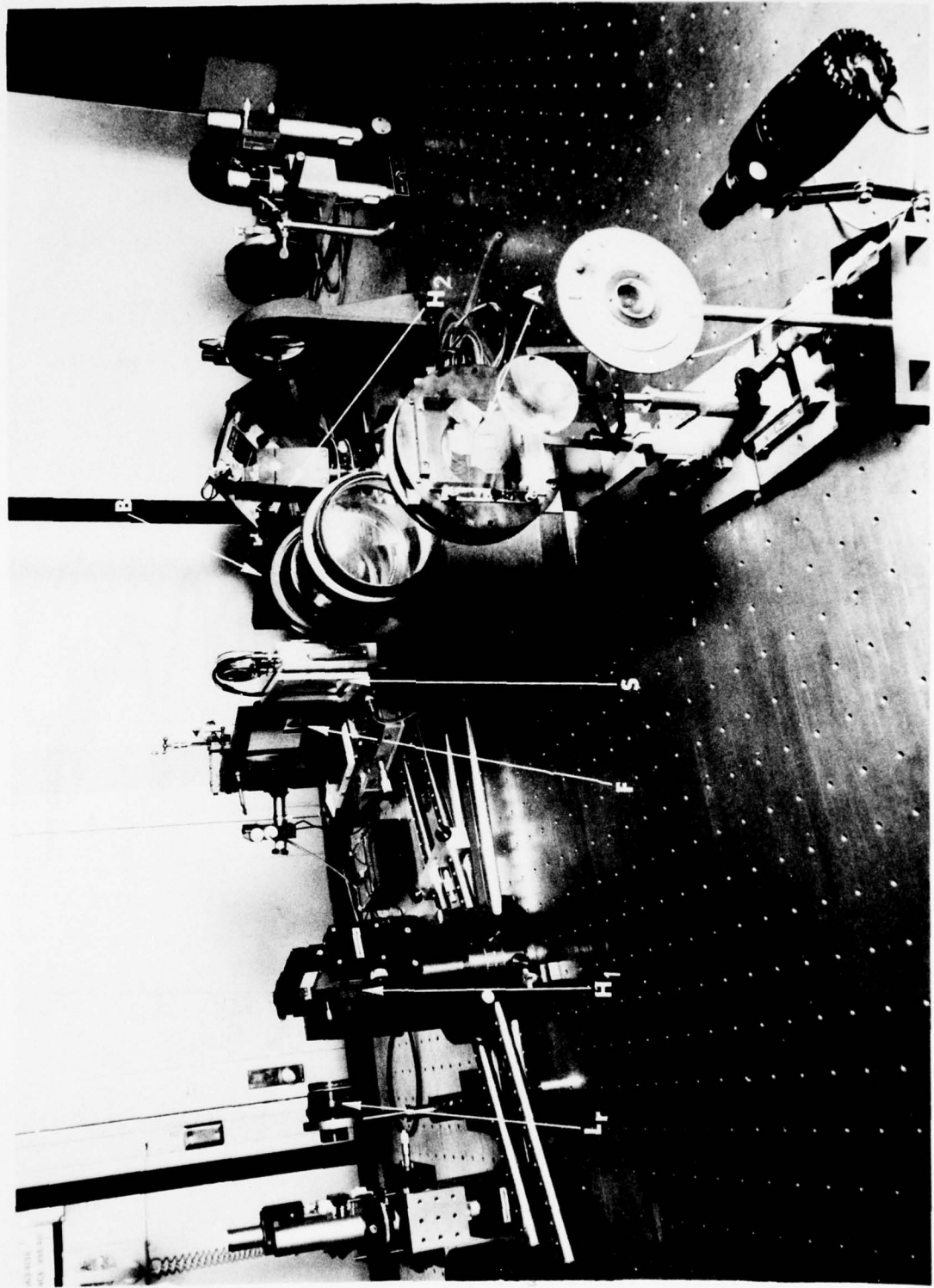


Figure 3. Real-time matched-filter optical processor using holographic optical elements.

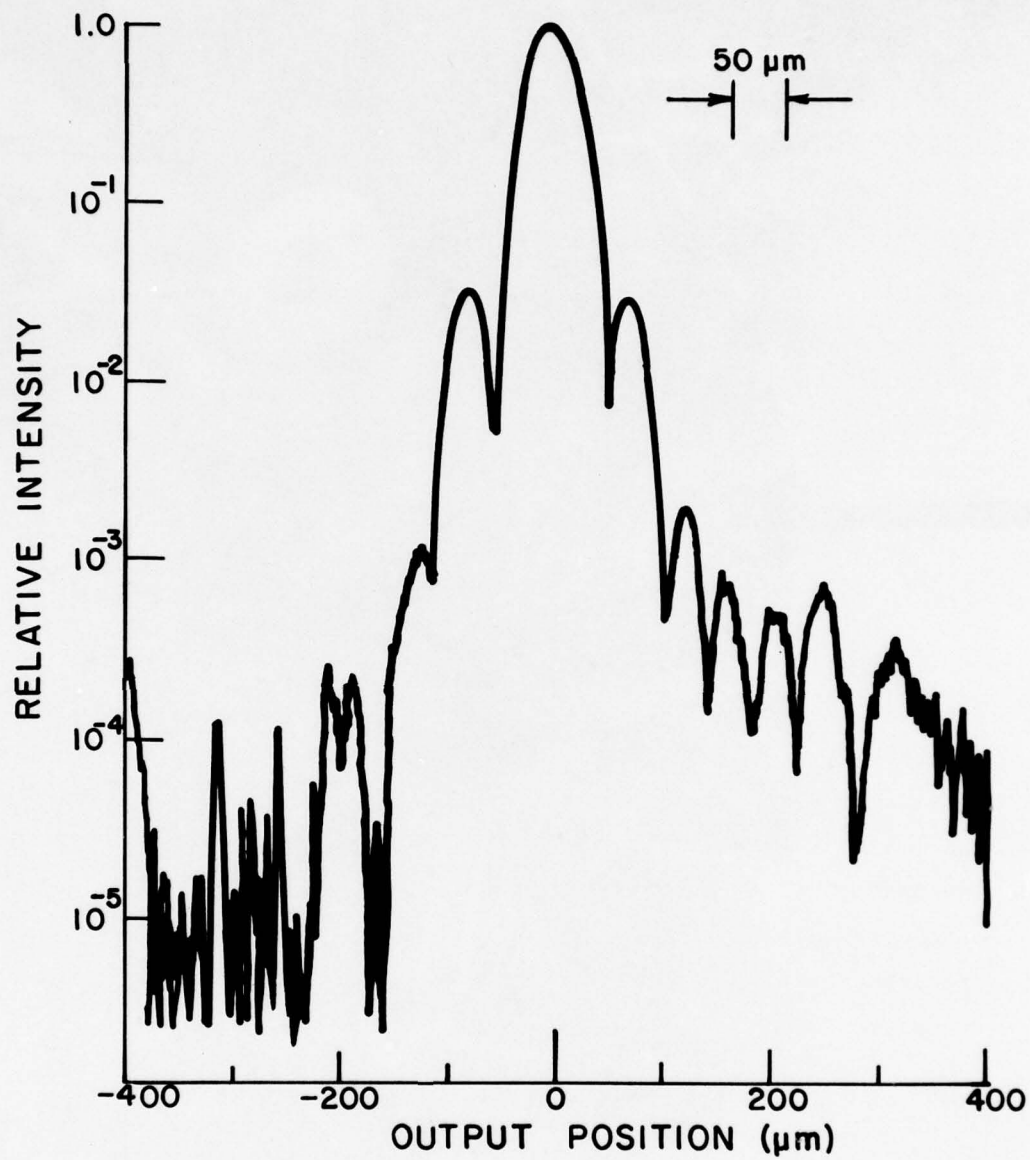


Figure 4. Scan through output of real-time matched filter optical processor.

were realized. The spot size is very close to the theoretically predicted diffraction-limited size of  $44\text{ }\mu\text{m}$  that would arise from the  $7.1\text{ mm}$  aperture used in the filter plane.

In this case, the performance of the holographic optics far exceeded the space-bandwidth product requirements of the input transducer, which was limited to  $200 \times 200$  picture elements due to the frequency of the grating sandwiched with the transparency. If the processor were made to be compact (using focal lengths of  $100\text{ mm}$  or less), then the performance of the holographic optics would more closely match that of the input transducer.

#### SAR DATA PROCESSOR

Synthetic aperture radar (SAR) optical data processors are another potential application for holographic optics. A holographic lens was used for Fourier transform processing of radar film. The resulting image compares favorably with an image produced by a conventional optical processor. The imagery, which is classified SECRET, is not included in this report. The potential light weight and compact design of holographic optics are attractive features for optical processors for airborne radar systems. The predicted performance of a simple holographic lens for two-dimensional Fourier transformations is given by Figure 6 of Appendix A.

#### CONCLUSIONS

Both analytical and experimental results obtained under this effort show that holographic optics perform well as the Fourier transforming lenses in optical processors. Images of moderate space-bandwidth product



can be processed by a very compact and light weight optical processing system using holographic lenses of a very simple design. If combined with a real-time incoherent-to-coherent transducer, such as the photo-conductor-thermoplastic device, holographic optics can be used to form a terrain-matching optical correlator suitable for terminal guidance applications. If longer focal lengths are allowed, then holographic lenses are capable of processing imagery of large space-bandwidth product.

The results of the analysis of the holographic lenses performed in this study was generally verified by the experimental results. The standard deviation phase error criterion developed for the matched-filter optical processor was found to be a useful guide for designing and analyzing holographic Fourier transforming lenses.

Further improvement in the performance of the holographic lenses could come in three areas: the use of multiple-element Fourier transform lenses, the use of holograms and output detectors on curved surfaces, and the use of holographic lenses recorded with nonspherical wavefronts.

Appendix A  
HOLOGRAPHIC OPTICS FOR A MATCHED-FILTER OPTICAL PROCESSOR

by

J. R. Fienup and C. D. Leonard

Environmental Research Institute of Michigan  
P. O. Box 8618, Ann Arbor, Michigan 48107

ABSTRACT

The requirements on and the performance of holographic Fourier transform lenses for a matched-filter optical processor are discussed. The holographic aberrations were analyzed using a ray-tracing computer program, and holographic lenses were fabricated and assembled into an optical processor. Analysis and experimental results show that holographic optics are capable of processing images of large space-bandwidth product and can be an attractive alternative to conventional optics.

(This work was supported by the Air Force Office of Scientific Research under Contract No. F44620-76-C-0047.)

## I. INTRODUCTION

Coherent optical processors have proven useful for a number of applications [1]. The unique properties of holographic optical elements offer a number of advantages over glass lenses for use in optical processors. Compared with conventional optics, holographic lenses are thin and light weight. Made by a photographic process, they are potentially inexpensive. They can be made in reflection as well as transmission, allowing for compact folded light paths. Additional advantages include the possibility of multiple functions in the same area of a given hologram (such as focusing, beam splitting, and spectral filtering), multiple superimposed holograms, the ability of a hologram on a curved surface to function independently of shape of the surface, and the ease of recording holographic elements with non-spherical wavefronts.

Reflection holograms recorded in dichromated gelatin can satisfy the requirements of an optical processor for high diffraction efficiency, high angular bandwidth, and low optical noise [2]. Dichromated gelatin holograms of good optical quality can diffract over 95% of the incident light into the first diffracted order and can have angular bandwidths of several degrees.

We analyzed the aberrations of holographic optics in a matched filter optical processor, and fabricated and tested an optical processor using holographic lenses. We found holographic lenses to perform well, and

conclude that they are an attractive alternative to conventional lenses for those applications that can benefit from their unique properties.

## II. ANALYSIS OF OPTICS FOR A MATCHED-FILTER PROCESSOR

For comparison, a conventional matched filter optical processor and its holographic optics counterpart are shown in Figure 1(a) and (b), respectively. As previously noted, the striking properties of the holographic optical processor are its compact folded geometry and its light weight. Referring to Figure 1, the input (signal) transparency  $S$ , which has amplitude transmittance  $s_1(x)$ , is illuminated by a plane wave from the collimator  $H_c$  (or  $L_c$ ). We use one-dimensional notation for simplicity; the extension to two dimensions is obvious. In the ideal case, the first Fourier transforming element  $H_1$  (or  $L_1$ ) causes the wavefront  $S_1(u) = \mathcal{F}\{s_1(x)\}$ , the Fourier transform of  $s_1(x)$ , to appear at the filter plane. The matched filter has been made to have an effective transmittance  $S_2^*(u) = (\mathcal{F}\{s_2(x)\})^*$  where  $s_2(x)$  is a reference image and  $(*)$  denotes the complex conjugate. The second Fourier transforming element (also referred to as the re-imaging element)  $H_2$  (or  $L_2$ ) causes the Fourier transform of  $S_1(u) S_2^*(u)$ , the wavefront emerging from the filter, to appear at the output plane OD. For simplicity, assume that the focal lengths of the two Fourier transforming elements are the same. The amplitude of the output is given by



$$g(x) = s_1(x) \star s_2(x)$$

$$= \int_{-\infty}^{\infty} s_1(x_1) s_2^*(x+x_1) dx_1 \quad (1)$$

which is the desired cross-correlation. In Eq. (1), constant factors that depend on optical parameters are ignored. If the input image is simply the reference image shifted so that it is centered at  $x_0$ , then the output becomes the autocorrelation

$$g(x) = \int_{-\infty}^{\infty} s(x_1) s^*(x+x_0+x_1) dx_1 \quad (2)$$

which has its peak at  $-x_0$ :

$$A_0 = g(-x_0) = \int_{-\infty}^{\infty} |s(x_1)|^2 dx_1 \quad (3)$$

$$= \int_{-\infty}^{\infty} |S(u)|^2 du$$

where the second line of the equation above results from Parseval's theorem.

As with conventional optics, holographic optics have aberrations that limit the performance of optical processors. For conventional optics, aberrations can be reduced by the use of well-designed multiple-element lens systems. However, a similar reduction of aberrations is usually not practical with holographic optics. Holographic elements ordinarily must be separated by a considerable distance in order to separate the desired order of diffraction from the spurious ones, although this effect is minimized by volume phase holograms. For reflection holograms, the element following the hologram cannot be allowed to block the beam incident on the hologram. Furthermore, due to their off-axis nature, a group of hologram lenses would be more difficult to align than on-axis optics. Besides, the use of multiple-element holographic optics would negate the advantages of light weight and low cost. For these reasons, we restricted our attention to simple single-element holographic lenses on plane substrates.

Unlike a simple lens with spherical surfaces, a holographic lens recorded with spherical wavefronts will introduce no phase errors if illuminated with the wavefront for which it was made. However, as the curvature and field angle of the incident wavefront differ from the reference beam used to record the hologram, aberrations appear, as analyzed by Champagne [3]. The chromatic aberrations are not a factor since the optical processor can operate with monochromatic light of the

same wavelength used to record the hologram. Since a hologram lens in an optical processor operates on a complex wavefront comprised of the sum of many wavefronts of various field angles, it necessarily exhibits aberrations [4]. The nonchromatic holographic aberrations are the limiting factor in the performance of the processor.

A. Standard Deviation Criterion

In order to specify the maximum tolerable aberrations that the Fourier transforming elements can be allowed to introduce, it is first necessary to determine, in general, the effects of aberrations in the Fourier transforming elements on the correlation output of the matched filter optical processor. However, due to the operation of the matched filter combined with the space variance of the aberrations, it is not possible to analyze the entire system by conventional wavefront analysis or ray-tracing methods. Therefore, it is necessary to simplify the analysis, say, by treating only one of the elements at a time. In order to judge a single Fourier transforming element, we used a standard deviation error criterion, which is derived below. This derivation applies to conventional as well as holographic optics.

Referring again to Figure 1, suppose that  $H_1$  introduces a phase error  $\phi_1(x)$ . Strictly speaking,  $\phi_1$  is a function not only of the hologram coordinate, but also of the coordinate,  $u$ , of the filter plane;

that is,  $\phi_1$  is space variant. We will continue this derivation with the simplification that  $\phi_1$  is space invariant; a justification for this simplification will be given later. A further simplification is that the phase error  $\phi_1$  is introduced near the input plane. This is strictly true for certain processor geometries and approximately true for slowly varying phase errors for the geometry of Figure 1. The justification of the latter simplification relies on the fact that slowly varying phase wavefronts change slowly as they propagate. Since the phase errors involved are, in fact, small and slowly varying, this is a good approximation. Thus, for a slowly varying phase error  $\phi_1$ , the wavefront arriving at the filter is proportional to

$$[S(u)\exp(-j \frac{2\pi}{\lambda f} ux_0)] * \mathcal{F} \{ \exp(j\phi_1) \} \quad (4)$$

where  $\lambda$  is the wavelength of light,  $f$  is the focal length of the Fourier transforming element,  $x_0$  is the translation of the center of the input from the optical axis, and  $*$  denotes convolution. This wavefront, multiplied by the filter function  $S^*(u)$ , is approximately an apodized plane wave (if no phase errors were present, its phase would be  $-2\pi ux_0/\lambda f$ ). It is Fourier transformed and brought to focus in the output plane



by  $H_2$ , which introduces a slowly varying phase error  $\phi_2$  (which depends on  $x_0$ ). The amplitude of the wavefront at the output is given by

$$g(x) = \mathcal{F}\left\{\left([S(u)\exp(-j \frac{2\pi}{\lambda f} ux_0)] * \mathcal{F}\{\exp(j \phi_1)\}\right) S^*(u)\exp(j \phi_2)\right\} \quad (5)$$

where aberrations introduced by the matched filter are ignored [5]. If no phase errors are present,  $\phi_1 = \phi_2 = 0$ , then Eq. (5) would reduce to Eq. (2).

The effects of phase errors  $\phi_2$  are made more clear by setting  $\phi_1 = 0$  in Eq. (5), which then reduces to

$$g(x) = \int_{-\infty}^{\infty} |S(u)|^2 \exp[j \phi_2(u)] \exp[-j \frac{2\pi}{\lambda f} u(x+x_0)] du \quad (6)$$

Evaluating at the central peak,  $x = -x_0$ , the ratio of the intensity of the central peak to its theoretical maximum value is

$$\begin{aligned}
 R &= \frac{|g(-x_0)|^2}{A_0^2} = \frac{\left| \int_{-\infty}^{\infty} |S(u)|^2 \exp[j \phi_2(u)] du \right|^2}{\left| \int_{-\infty}^{\infty} |S(u)|^2 du \right|^2} \\
 &= \left| \sum_{k=0}^{\infty} \frac{(j)^k}{k!} \cdot \frac{\int_{-\infty}^{\infty} |S(u)|^2 \phi_2^k(u) du}{\int_{-\infty}^{\infty} |S(u)|^2 du} \right|^2 \\
 &= \left| \sum_{k=0}^{\infty} \frac{(j)^k}{k!} \overline{\phi_2^k} \right|^2
 \end{aligned} \tag{7}$$

where  $\overline{\phi_2^k}$  is a weighted average of the  $k^{\text{th}}$  power of  $\phi_2(u)$ . The weighting function  $|S(u)|^2$  is simply the intensity pattern of the wavefront emerging from the spatial filter. For reasons described later,

this weighting function can be approximated by a constant over the width of the filter. For small phase errors, assuming  $\overline{\phi^k} \ll 1$  for  $k \geq 3$ , Eq. (7) becomes

$$R \approx 1 - \overline{\phi_2^2} + \overline{\phi_2^2}^2 = 1 - \sigma_2^2 \quad (8)$$

where

$$\sigma_2 = \sqrt{\overline{\phi_2^2} - \overline{\phi_2}^2} \quad (9)$$

is the standard deviation of the phase error. That is, for small phase errors, the autocorrelation peak intensity is independent of the type of phase error present, and depends only on  $\sigma_2$ . This relationship between the normalized intensity and the standard deviation (sometimes loosely referred to as the rms) of the phase error is the familiar formula for the Strehl intensity. This is expected since the function of  $H_2$  is essentially to bring to focus a point-like image. Linear phase errors introduced by  $H_2$  shift the peak in the output plane (distortion) without degrading the peak itself. Since slight position errors may be acceptable or calibrated

out of the system, linear phase errors should not be included in the calculation of  $\sigma_2$ .

The effects of phase error  $\phi_1$ , introduced by the first Fourier transforming element  $H_1$ , are made more clear by setting  $\phi_2 = 0$  in Eq. (5), which then reduces to

$$g(x) = \int_{-\infty}^{\infty} s(\xi) \exp[j\phi_1(\xi+x_0)] s^*(\xi+x_0+x) d\xi \quad (10)$$

Evaluating at the peak,  $x = -x_0$ , this becomes

$$g(-x_0) = \int_{-\infty}^{\infty} |s(\xi)|^2 \exp[j\phi_1(\xi+x_0)] d\xi \quad (11)$$

Again expanding the exponential and interpreting the integral as a weighted sum of the phase errors, we find that for small phase errors,

$$R \approx 1 - \sigma_1^2 \quad (12)$$



where  $\sigma_1 = \left( \overline{\phi_1^2} - \overline{\phi_1}^2 \right)^{1/2}$  is the standard deviation of the phase error introduced by  $H_1$ . Unlike  $\sigma_2$ ,  $\sigma_1$  includes the contributions from linear terms. Thus, the normalized peak intensity of the autocorrelation output of a matched filter optical processor decreases with the square of the standard deviation of the phase error not only for the second re-imaging Fourier transforming element, but also for the first Fourier transforming element. This relationship allows the use of a very simple quality criterion for evaluating the Fourier transforming elements for a matched filter optical processor.

The approximations assumed in the derivation of Eq. (5) were that  $\sigma_1$  be small, slowly varying, and space-invariant. While  $\sigma_1$  generally will be small and slowly varying, it will not be space-invariant. In most cases,  $\sigma_1$  increases with increasing field angles, or, equivalently, with increasing  $|u|$  in the filter plane, and is maximum for  $u$  coordinates at the edge of the filter plane. The justification for the space-invariance approximation is as follows. Since the purpose of the matched filter optical processor is to produce a sharp peak in the output plane, it is the value of  $\sigma_1$  for points near the edge of the filter plane that determines the performance of the processor. Using  $\sigma_1$  at the edge of the filter is appropriate, since the information at the edges of the matched filter is ordinarily emphasized in order to increase the selectivity of the filter and increase the sharpness of the autocorrelation peak [6]. This is usually unavoidable

since it is difficult to record the large dynamic range of  $S^*(u)$  in the matched filter; but it is also highly desirable. The wavefront emerging from the matched filter has an intensity distribution that is more nearly constant or of an annular shape, rather than being sharply peaked in the center as  $|S(u)|^2$  would be. In this case, the output is no longer truly an autocorrelation; it more closely resembles a point image. Thus, we are led to base our analysis of the performance of element  $H_1$  on the value of  $\sigma_1$  for field angles corresponding to the edges of the filter.

A further justification of basing the analysis on  $\sigma_1$  at the edge of the filter is as follows. Suppose that for a given input size and system design,  $\sigma_1$  goes beyond a certain critical level (the value of that critical level will be shown later) for positions in the filter plane with  $|u| > |u_{\max}|$ . Then an aperture should be placed at the filter plane to block out the portion of the wavefront for which  $|u| > |u_{\max}|$ , since that portion of the wavefront will lead to a degradation rather than a reinforcement of the autocorrelation peak at the processor output. That value of  $|u_{\max}|$  defines the size of the filter used and, consequently, the maximum spatial frequency component of the input transparency that is used. Thus, the maximum usable space-bandwidth product of the input and the resolution at the output is determined by the value of  $|u_{\max}|$  for which  $\sigma_1$  goes above the critical level. One can therefore ignore the space variance of the phase error  $\phi_1$  and concentrate on the value of  $\sigma_1$  as computed for the edge of the matched filter.

To test the validity of Eq. (12) and to more accurately establish the effects of phase errors  $\phi_1$ , we digitally computed the aberrated autocorrelation integral of Eq. (5) with  $\phi_2 = 0$  for the hypothetical one-dimensional object shown in Figure 2(a) with various phase errors  $\phi_1$ . Figure 2(b) shows the central portion of the autocorrelation output with no phase error (uppermost curve) and with  $\sigma_1 = 1/16$  wavelength  $n^{\text{th}}$ -order phase error for  $n = 1$  to 4, respectively. That is, one curve results from a linear phase error of .2165 wavelengths peak-to-peak, the second from a quadratic phase error of .2097 wavelengths, etc. The peaks of all four curves fall into the range of 0.842 to 0.868, in very good agreement with the value  $1 - (2\pi/16)^2 = 0.846$  predicted by Eq. (12). Figure 2(c) shows the same thing with  $\sigma_1 = 1/8$  wavelength. In this case, the peaks fall in the range 0.478 to 0.567, not in very good agreement with the value 0.383 predicted by Eq. (12). Figure 2(d) shows the same thing with  $\sigma_1 = 1/4$  wavelength. From Figures 2(c) and 2(d), it is apparent that Eq. (12) is no longer reliable for  $\sigma_1 \geq 1/8$  wavelength. However, for  $\sigma_1$  much greater than  $1/8$  wavelength the autocorrelation peak would no longer be detectable.

From the above results, we can formulate the following standard deviation phase error criterion: the standard deviation of the total phase error should be kept to  $1/8$  wavelength in order to insure that the autocorrelation peak remain easily detectable. This corresponds to the following peak-to-peak errors (in wavelengths): .433 of linear, .419 of quadratic,

.660 of cubic, and .468 of fourth-order. As shown in Figure 2(c),  $\sigma_1 = 1/8$  wavelengths results in a greatly reduced, but still detectable, autocorrelation peak; and as shown in Figure 2(d),  $\sigma_1 = 1/4$  wavelengths results in an autocorrelation peak that would be lost in the noise.

As discussed earlier, it is desirable to record the matched filter in a nonlinear way so as to block the lower and emphasize the higher spatial frequencies. In a computer simulation, this effect was approximated in Eq. (5) by multiplying  $S^*(u)$  by a high-pass stop of the form  $[1 - \text{rect}(u/u_a)]$ . As expected, this resulted in an output peak that is much sharper and has a higher signal-to-noise ratio. An example of this is shown in Figure 2(e), for which  $\sigma_1 = 0$  and the high-pass stop was 20% of the total filter-plane aperture width. Figure 2(f) shows the results with  $\sigma_1 = 1/4$  wavelength  $n^{\text{th}}$  order phase error for  $n = 1$  to 4, respectively. Since the output peaks are easily detectable above the noise, these curves suggest that the emphasis of the higher spatial frequencies also serves to make the process less sensitive to the slowly varying phase errors. Thus, the standard deviation phase error quality criterion developed above for the case of linear filter recording should be taken as a lower bound on the performance of the Fourier transforming lens.

#### B. Aberration Computation

Champagne's equations [3] can be used to compute the third-order



holographic aberrations, but they are inconvenient for computing the standard deviation phase error,  $\sigma$ . Furthermore, they do not include higher-order aberrations without adding considerable complexity. Consequently, to accurately and efficiently analyze and optimize the design of the holographic optics, we used a holographic ray-tracing computer program called the Holographic Optics Analysis and Design (HOAD) program, developed at ERIM [7].

The hologram  $H_c$  shown in Figure 1(b) is a collimator and is reconstructed in exactly the same way that it was recorded. Consequently, it has no holographic aberrations and produces an ideal plane wave.

In analyzing  $H_1$ , the first Fourier transforming element, it is important to note that, whatever aberrations  $H_1$  introduces, if the same element is used to record the matched filter, then it is a matched filter of an aberrated reference image. If the untranslated reference image is used as the input, and the same aberrations are introduced, then it should correlate perfectly. This would seem to indicate that a very poor lens could be used for  $H_1$ , and indeed, that is the case if the image is not translated in the input. However, as the input is translated, the effective aberrations change, and the correlation peak degenerates. Thus, the phase error of interest is not the absolute phase error, but is the difference between the phase error when the center of the input image is translated to  $x_0$  and the phase error when the center of the image is on the optical axis (i.e., as the matched filter was recorded). Consequently,

some of the requirements for the Fourier transforming lens, for example, that the Abbe sine condition must be fulfilled [8], may be relaxed. Generally, the phase error differences are minimized when the absolute phase error is minimized, and low-aberration lenses are required for the matched filter optical processor.

To analyze  $H_1$ , we considered one plane-wave spatial frequency component of the input at a time, by tracing crossed fans of parallel rays at a given field angle from the input plane, through  $H_1$ , to the filter plane. Often the translation,  $x_o$ , of the input image relative to the reference image is comparable in size to, or larger than, either the input image or the reference image (in many applications, one of the two images covers a much smaller area than the other — we refer to the smaller of the two as the "image of interest"). In that case, the predominant term in the difference of the phase errors is a linear term. That is, the predominant effect is that if a plane-wave component of the image comes to focus at  $u_1$  when the image is centered on the optical axis, then it will come to focus at  $u_1 + \Delta u$  when the image is centered at  $x_o$ ; and the linear phase term is proportional to  $\Delta u$ . The difference of the phase errors can be approximated by computing the aberrations of the plane-wave component of the input image with respect to the position  $u_1$  in the filter plane (rather than computing the aberrations with respect to its own image point at  $u_1 + \Delta u$ ).

The analysis of  $H_2$  is simpler, since it only brings a quasi-plane wave to focus at the output, and linear phase errors are not considered significant. Because of this, the requirements on  $H_2$  are not as stringent as on  $H_1$ , nor are they as stringent as they would be for some other types of processors.

### C. Optimization and Analysis

Holographic optics has a somewhat different set of parameters for design optimization than is available to conventional optics. The overall geometry of a holographic optical system can be adjusted by appropriate choices of focal lengths, offset angles, and transmissive vs. reflective holograms. Since the gross imaging properties of an individual holographic element do not depend on the angular orientation or shape of its surface, the angular orientation of the element with respect to the rest of the system and the curvature of the surface of the hologram substrate can be designed to minimize aberrations. A hologram can be made at one wavelength and read out at a second wavelength. The thickness and refractive index modulation of a holographic element can be manipulated to produce a desired Bragg angular and wavelength selectivity. Analogous to conventional lenses, holographic elements of a given focal length can have different shape factors, depending on the curvatures of the reference and object beams used to record the hologram.

In general, aberrations tend to be minimized when the offset angles

are minimized, so the minimum offsets allowed by the system geometry were used. It was assumed that the processor operates at the same wavelength, 514.5 nm, at which the holograms are recorded, which also tends to minimize aberrations. In order to keep the system as simple and economical as possible, only single elements on plane surfaces were considered.

### 1. Before-the-Lens Processor

Using the HOAD program, we optimized the shape factors of  $H_1$  and  $H_2$  and their angular orientations with respect to the rest of the system. As depicted in Figure 1(b),  $H_1$  and the filter should be parallel to one another and normal to the axis between them. Similarly,  $H_2$  and the output plane should be parallel to one another, and normal to the axis between them. (Note that the input plane S is parallel to  $H_1$ , as shown, making it tilted with respect to the S- $H_1$  axis. If S is rotated to be normal to the S- $H_1$  axis, then the output plane OD rotates to become parallel to S, but tilted with respect to the  $H_2$ -OD axis.) The recording geometry for  $H_1$  is shown in Figure 3 for a  $10^\circ$  offset, where the point source for the object beam is located at the center of the filter plane and the reference beam is a plane wave conjugate to the S- $H_1$  axis. The recording geometry of  $H_2$  is the mirror image of Figure 3, where the point source for the object beam is located at the center of the output plane and the reference beam is a plane wave conjugate to the filter -  $H_2$  axis.



The HOAD program was used to compute  $\sigma_1$ , the standard deviation phase error of  $H_1$ , as a function of field angle (or filter plane location), diameter  $D_s$  of the image of interest, translation  $x_o$  of the input, and focal length. The performance can be determined, for example, by fixing all the parameters except  $x_o$ , then increasing  $x_o$  until  $\sigma_1$  equals  $1/8$  wavelength. This, along with the diameter of the image of interest, defines  $D = D_s + 2x_o$ , the greatest width of an image that can be processed, that is, within which the image of interest can be located and still produce a detectable correlation peak. Combined with the field angle (corresponding to the maximum spatial frequency component of the image), the width gives the maximum space-bandwidth product (number of picture elements) that can be processed without a loss of resolution.

Two families of operating curves for a 100 mm focal-length  $H_1$  are shown in Figure 4. The varying parameters for the different curves are  $D_s$  and the maximum spatial frequency, respectively. These curves may be used as follows. If it is required that the resolution of the matched filtering operation be equivalent to 20 cyc/mm in the input plane, and that the image of interest be detectable anywhere within a total image area of  $750 \times 750$  picture elements, then the image of interest could contain no more than  $100 \times 100$  picture elements. Two facts made evident by Figure 4 are that the performance improves if the image is demagnified (i.e., it performs better for higher spatial frequencies, but proportionally

smaller image widths), and that there is a trade-off between  $D_s$  and  $D$  (i.e., the larger the image of interest, the less it can be translated).

The aberrations of the second Fourier transforming element,  $H_2$ , were also computed. Since it was found that the aberrations of  $H_1$  generally were the limiting factor in the performance of the system, the less interesting results on  $H_2$  will not be given here.

A most important parameter is the focal length,  $F$ , of the Fourier transforming elements. Using Champagne's equations [3], it can be shown that, for a given image size and field angle, third-order coma is proportional to  $1/F^2$ , and third-order astigmatism is proportional to  $1/F$ . Consequently, the performance of the processor improves greatly with increasing focal lengths. As an example, Figure 5 shows the translation  $x_0$  that results in  $\sigma_1 = 1/8$  wavelength vs. focal length, for various values of  $D_s$ . A highest spatial frequency of 40 cyc/mm and an offset of  $10^0$  was assumed. In this case, 10 mm is equivalent to 800 picture elements. Figure 5 indicates that a compact processor using elements with short (100 mm) focal lengths can process imagery of a few hundred picture elements on a side; and if long ( $> 1$  meter) focal lengths are allowed, then the holographic optics can handle imagery having thousands of picture elements on a side.

## 2. After-the-Lens Processor

An alternative to the configurations shown in Figure 1 is to locate

the input plane in a converging beam after a transmissive first Fourier transforming lens [5], which would allow for easy changes in scale by translating the input along the optical axis. In this case, the first Fourier transforming element, which could be combined with the collimator, would produce a perfect converging spherical wavefront. Nevertheless, the resulting Fourier transform would be aberrated (in addition to having a spherical phase factor associated with the Fourier transform).

In order to analyse the aberrations of the after-the-lens Fourier transform geometry, consider a single spatial frequency component of the input. For this analysis, we use Champagne's notation and equations [3], in which  $R$  is the radial distance of a recording or reconstruction point source from the hologram,  $\alpha$  and  $\beta$  are field angles, and subscripts  $R$ ,  $O$ ,  $C$ , and  $I$  refer to reference, object, reconstruction, and image beams, respectively. The input then can be modeled as a constant-frequency holographic grating with recording parameters  $R_R = R_O = +\infty$ ,  $\alpha_R = \beta_R = 0$ , and  $\alpha_O$  and  $\beta_O$  are the angles corresponding to the spatial frequency under consideration. For simplicity, consider  $\beta_O = 0$ , since the performance will be symmetric in the  $x$  and  $y$  dimensions. The reconstruction beam is a spherical wave converging to the center of the matched filter plane, and is given by  $R_C = -F$  and  $\alpha_C = \beta_C = 0$ . Then Champagne's equations for the image

location reduce to

$$R_I = R_C = -F \quad (13)$$

$$\sin \alpha_I = \sin \alpha_0, \text{ or, } \alpha_I = \alpha_0 \equiv \alpha \quad (14)$$

and

$$\cos \alpha_I \sin \beta_I = \cos \alpha_C \sin \beta_C = 0 ; \quad (15)$$

and the coefficients of the third-order aberrations reduce to

$$S = \frac{1}{R_C^3} - \frac{1}{R_I^3} = 0 \quad (16)$$

$$C_x = \frac{\sin \alpha_I}{R_I^2} = - \frac{\sin \alpha}{F^2} \quad (17)$$



$$C_y = 0 \quad (18)$$

$$A_x = -\frac{\sin^2 \alpha_I}{R_I} = -\frac{\sin^2 \alpha}{F} \quad (19)$$

and

$$A_y = A_{xy} = 0 \quad (20)$$

where the coefficients  $S$ ,  $C$ , and  $A$  are for aberrations of the spherical, comatic, and astigmatic types, respectively.

It is interesting to compare these aberrations with those of the before-the-lens processor. For the before-the-lens processor, using the holographic element shown in Figure 2, the recording parameters are  $R_R = -\infty$ ,  $R_O = F$ ,  $\alpha_R = 10^\circ$ , and  $\beta_R = \alpha_O = \beta_O = 0$ ; and for the reconstruction,  $R_C = \infty$ , and  $\alpha_C$  and  $\beta_C$  are variable. If  $\beta_C$  is set to zero and  $\sin \alpha$  is substituted for  $\sin \alpha_C - \sin \alpha_R$ , then it can be shown that the aberration coefficients of the optimized holographic before-the lens processor are exactly the same as those given above for the after-the-lens processor. The aberrations in

the two cases are not exactly the same, however, since a given plane wave spatial frequency component of the input to the before-the-lens processor arrives at  $H_1$  off center by a distance  $F \sin \alpha$ . Nevertheless, using the HOAD program it was found that, for the range of parameters of interest, the performance of the after-the-lens processor is nearly identical to that of the holographic before-the-lens processor.

In addition to allowing scale changes, the after-the-lens processor allows for a distance of  $F$  between the input and filter planes, as compared to  $2F$  for the before-the-lens processor (this advantage is diluted, however, since the before-the-lens processor can be folded to reduce the  $2F$  length back to  $F$ ). Furthermore, for longer focal length systems for which  $\alpha F$  is comparable to  $D$ , the Fourier transforming element in the after-the-lens processor can be smaller than that of the before-the-lens processor. A possible disadvantage of the after-the-lens processor is that since the matched filter is required to record an additional spherical phase factor, the matched filter itself will introduce aberrations not present in the matched filter made for a before-the-lens processor [5,9].

### 3. Fourier Spectrum Analysis

The holographic Fourier transforming lenses were also analyzed for use in simple Fourier transform optical processors, for performing Fourier spectrum analysis of an input transparency. Such a processor would be similar to

the first half of the matched-filter optical processor, with the output plane being located in place of the matched filter. For this analysis, the distortion of the output (linear phase errors) was ignored, and it was assumed that the optimized holographic lens shown in Figures 3 with a  $10^\circ$  offset angle is used, and it was required that  $\sigma$  not exceed  $1/8$  wavelength at 40 cyc/mm in the input. Figure 6 shows the predicted linear space-bandwidth product of the input that could be Fourier transformed (which is proportional to the maximum allowed width of the input) as a function of the focal length of the holographic lens.

### III. HOLOGRAM FABRICATION

Dichromated gelatin plates were prepared by fixing the silver halide out of  $5 \times 5$  inch Kodak 649-0 microflat plates, then sensitizing with ammonium-dichromate solution. The processing procedures used were those of Chang and Colburn [2], which are similar to those of Chang [10]. Due to the physical sizes of the plate holders and other available equipment, we chose the focal lengths and offset angles of the two Fourier transforming lenses to be 500 mm and  $20^\circ$ , respectively. Using the 514.5 nm wavelength from an argon-ion laser, typical exposures were at  $1 \text{ mW/cm}^2$  for eight minutes.

The emulsion side of the plate was placed away from the point source during recording and away from the input and filter planes when in the processor. Consequently, the input wavefront passes through the glass

substrate both before and after reflection from the holographic lens. The spherical aberration introduced by the glass substrate into the diverging recording beam is cancelled by the opposite aberration introduced by the substrate into the converging reflected wavefront upon readout. An advantage of this orientation of the emulsion is that the reconstructed beam is reflected without passing through the outer surface of the emulsion. Then the dichromated gelatin hologram can be sealed (to protect the emulsion primarily from the effects of humidity) by cementing on a thin glass cover plate, without having to consider the optical quality of the cover plate.

The diffraction efficiency of a typical holographic lens made for the experiments is 70%. Heavier exposures resulting in higher diffraction efficiencies were avoided since they also result in the recording of spurious holograms. The spurious holograms arise from beams internally reflected from the air-glass and air-gelatin surfaces. For the highest quality results, those unwanted reflections can be eliminated by recording the hologram in a liquid gate with antireflection windows.

The diffraction efficiency of the holographic lenses must remain high for a range of angles of illumination. For the first Fourier transforming lens, the required angular bandwidth is  $\pm \alpha_m$ , where  $\alpha_m$  is the angle corresponding to the maximum spatial frequency of the input; for example,  $\alpha_m = 1.18^\circ$  for a frequency of 40 cyc/mm. For the second Fourier



transforming lens, the required angular bandwidth is  $\pm \arctan (x_m/F)$ , where  $x_m$  is the largest allowed translation of the input; for example, if  $x_m/F = 25 \text{ mm}/500 \text{ mm}$ , then the required angular bandwidth is  $\pm 2.86^\circ$ . The angular bandwidths of the holographic lenses were made to easily satisfy these requirements, as can be seen from the curves shown in Figure 7 of diffraction efficiency versus angle of illumination for the central portions of two different holographic lenses. Both holographic lenses were recorded with  $20^\circ$  offset angles and are designed to operate at angles about  $20^\circ$ . The double peaks in curve A arise from the symmetry of the Bragg condition about the angle of approximately  $10^\circ$  to which the fringe planes are normal. The right peak of curve A is at an angle greater than  $20^\circ$  due to an increase in the thickness of the hologram emulsion. A decrease in the emulsion thickness caused the peaks of curve B to move together to form a single broad peak. The emulsion thickness is controlled primarily by the concentration of the sensitizer. The thickness can then be fine-tuned during the drying process in which the holograms are baked in an oven under vacuum, which drives moisture from the emulsion. The emulsion thickness can be decreased by additional baking. If the emulsion is baked excessively and becomes too thin, then it can be made thicker by immersing it in water and baking it again to a lesser degree. In this way the peak of the angular selectivity curve can be adjusted as desired, within certain limits.

The high angular bandwidths of the holographic lenses result from large refractive index modulations, determined to be approximately 0.07. Higher modulation could be achieved, but at the expense of optical quality.

Our primary consideration was the phase aberrations of the holographic lenses. Before preparing them for exposure, the best samples from a few boxes of 649-0 plates were selected, based on examination of flatness using a Mach-Zehnder interferometer. Since washing and sensitization of the plates was done after the interferometric test, it did not matter that the plates were exposed to light during the test. After being recorded and processed, the holograms were tested for aberrations using the interferometer geometry shown in Figure 8. The position of the point source illuminating the hologram was the same as that used to record it and so there are no theoretical holographic aberrations. The aberrations that appear in this configuration (the "non-holographic aberrations") are due, primarily, to variations in emulsion thickness and edge effects. Figure 9 shows interferograms of diameter 10 cm of two different holographic lenses used in our experiments. The peak-to-peak phase error of lens A is about  $\lambda/4$  over a 4 cm diameter and  $\lambda/2$  over an 8 cm diameter, and of lens B is about  $\lambda/4$  over a 4 cm diameter and about  $\lambda/2$  over a 6 cm diameter. These aberrations are sufficiently low for the purposes of our experiments.

#### IV. CORRELATION EXPERIMENTS

The holographic lenses described in the previous section were

assembled into a matched filter optical processor, and matched filtering experiments were performed. Matched filters on  $4 \times 5$  inch Kodak 131-01 microflat plates were recorded with the image centered in the input plane and using  $H_1$  to perform the Fourier transform; referring to Figure 1(b), the reference beam was a plane wave along the filter-to- $H_2$  axis. The intensities of the reference and signal beams were adjusted so that the fringe contrast was highest for spatial frequencies above 15 cyc/mm. This resulted in matched filters that are opaque in their central regions because of heavy overexposure. The filters, giving heavy weighting to the higher spatial frequencies, resulted in very sharply peaked "correlation" outputs [6].

In one experiment, the matched filter was recorded of a 25 mm diameter area of the input image shown in Figure 10. The filter was limited to a 13.5 mm diameter aperture, corresponding to a field angle of  $0.77^\circ$  and a spatial frequency of 26 cyc/mm. The central 3.5 mm diameter area of the filter was opaque, resulting in an active area of the filter having an annular shape. A photometric scan through the correlation peak for  $x_0 = 4$  mm is shown in Figure 11. The half-power width of the peak shown is about  $31 \mu\text{m}$  and it is more than 30 dB above the noise. The sidelobe ring around the main peak is a characteristic of the annular shape of the matched filter. The intensity of the correlation peak as a function of input translation  $x_0$  is shown in

Figure 12. Even at  $x_0 = 21$  mm, for which its intensity is 15% of its value for  $x_0 = 0$ , the peak, though aberrated, is easily detectable and is 28 dB above the noise, as shown in Figure 13.

The performance of the holographic optics indicated by the results above is somewhat better than that predicted by the standard deviation phase error criterion. For an input of diameter 25 mm and a field angle of  $0.77^\circ$ , the HOAD program predicts  $\sigma_1 = 1/8$  wavelength for  $x_0 = 10$  mm; but the measured peak intensity does not drop to 50% until  $x_0 = 13.5$  mm, and is easily detectable for  $x_0$  beyond 21 mm. This discrepancy is due to the inaccuracy of the space invariance assumption and the decreased sensitivity of the processor to slowly varying phase errors when the higher spatial frequency information is emphasized. Thus, the standard deviation phase error criterion should be taken as a lower bound on the performance of the processor.

## V. IMAGING EXPERIMENT

Another test of the holographic Fourier transform lenses was to use one as the first element in a two-lens imaging system, as shown in Figure 14. A bar target in the front focal plane of holographic lens  $H_1$  was illuminated with light made spatially incoherent by a rotating diffuser (used in order to eliminate speckle in the image). An aperture of diameter 44 mm was placed in the back focal plane of  $H_1$  and in the front focal plane of the reimaging lens  $L_c$ , which was designed as a collimating lens. The orientations of  $H_1$  and  $L_c$  were such that diffraction-



limited imaging was expected for the point at the center of the image. The ratio of the focal lengths of  $L_c$  and  $H_1$ , being 300 mm/500 mm, gave a net magnification of 0.6. Figure 15(a) shows the resulting image. Figure 15(b) shows a magnified portion of the center of the image, where the finest resolved bar separation at the input target is seen to be about 7  $\mu\text{m}$ , which is roughly equal to the diffraction limit of  $1.22 \lambda F / 44 \text{ mm} = 7.1 \mu\text{m}$ . Figure 15(c) shows a magnified portion of one edge of the image, where the finest resolved bar separation is about 8  $\mu\text{m}$  vertically and 11  $\mu\text{m}$  horizontally. Assuming a perfect Fourier transforming lens for  $L_c$ , the HOAD program predicted a geometrical spot of rms diameter 28  $\mu\text{m}$  for that location in the image, considerably worse than that obtained experimentally. This resulted from the fact that the collimating lens  $L_c$ , a doublet, does not perform a perfect Fourier transform, and its aberrations partially compensate for the aberrations of the holographic lens.

## VI. CONCLUSIONS

Analysis was performed and experiments verified that holographic optics can perform well as the Fourier transforming elements of a matched-filter optical processor. The aberrations of a holographic before-the-lens processor were found to be comparable to those of an after-the-lens processor. Holographic optics of a simple design are

capable of processing imagery of large space-bandwidth product if long enough focal lengths are allowed. The standard deviation phase error criterion was found to be a useful guide for predicting the performance of the lenses in a matched-filter optical processor.

This work was supported by the Air Force Office of Scientific Research under Contract No. F44620-76-C-0047.

## REFERENCES

1. A. Vander Lugt, "Coherent Optical Processing", Proc. IEEE 62, 1300 (1974).
2. B. J. Chang and W. S. Colburn, to be submitted for publication.
3. E. B. Champagne, "Nonparaxial Imaging, Magnification and Aberration Properties in Holography", J. Opt. Soc. Am. 57 (1967); E.B. Champagne, "A Qualitative and Quantitative Study of Holographic Imaging", Ph.D. Thesis, Ohio State University, Columbus, Ohio, July 1967 (University Microfilms, No. 67-10876).
4. This point was not understood by P.C. Mehta, S. Swami, and V.V. Rampal, "Compact Optical Data Processor Employing Holographic Reflective Lenses", Appl. Opt. 16, 445 (1977); consequently, their estimate of processing capabilities of  $10^{10}$  bits is grossly overstated.
5. A. Vander Lugt, "Practical Considerations for the Use of Spatial Carrier-Frequency Filters", Appl. Opt. 5, 1760 (1966).
6. D. J. Raso, "Simplified Method to Make Hologram Filters for Target Recognition", J. Opt. Soc. Am. 58, 432 (1968).
7. J. N. Latta, "Computer Based Analysis of Holography Using Ray-Tracing", Appl. Opt. 10, 2698 (1971); J.N. Latta and R. C. Fairchild, "New Developments in the Design of Holographic Optics", Proc. of the SPIE 39, Applications of Geometrical Optics, 107 (1973).
8. K. von Bieren, "Lens Design for Optical Fourier Transform Systems", Appl. Opt. 10, 2739 (1971).
9. M. J. Bage, and M. P. Beddoes, "Lenseless Matched Filter: Operating Principle, Sensitivity to Spectrum Shift, and Third-Order Holographic Aberrations", Appl. Opt. 15, 2830 (1976).
10. M. Chang, "Dichromated Gelatin of Improved Optical Quality", Appl. Opt. 10, 2550 (1971).

## LIST OF FIGURES

1. Configurations of optical processors using (a) conventional optics and (b) holographic optics.
2. Computer simulation of matched filter output with aberrations. (a) test object, (b)-(f) central portions of aberrated autocorrelation outputs: (b) no phase error (uppermost curve) and  $\sigma_1 = \lambda/16$   $n^{\text{th}}$  order phase error,  $n = 1$  to 4; (c)  $\sigma_1 = \lambda/8$ ; (d)  $\sigma_1 = \lambda/4$ ; (e) 20% central stop, no phase error; (f) 20% central stop,  $\sigma_1 = \lambda/4$ .
3. Recording geometry for  $10^\circ$  offset Fourier transforming holographic lens.
4. Performance of 100 mm focal length Fourier transforming holographic lens: the linear space-bandwidth product of the total image vs. the linear space-bandwidth product of the area of interest, for various values of the width ( $D_s$ ) of the area of interest and of the maximum spatial frequency of the image.
5. Translation  $x_o$  of the input resulting in  $\sigma_1 = \lambda/8$ , versus focal length ( $F$ ), for various widths ( $D_s$ ) of the image of interest. A  $10^\circ$  offset and 40 cyc/mm spatial frequency are assumed, making 10 mm equivalent to 800 picture elements.
6. Performance of holographic lens for Fourier spectrum analysis, assuming  $\sigma \leq \lambda/8$  at 40 cyc/mm.
7. Diffraction efficiency vs. angle of illumination for holographic lenses A and B.
8. Interferometer for testing holographic lenses.
9. Interferograms of holographic lenses A and B.
10. Input image for correlation experiments.
11. Scan through peak of output,  $x_o = 4$  mm.
12. Intensity of output peak vs.  $x_o$ .
13. Scan through peak of output,  $x_o = 21$  mm.
14. Imaging system using a holographic lens.
15. Output image. (a) Entire field-of-view; (b) Magnified central area; (c) Magnified right side area.



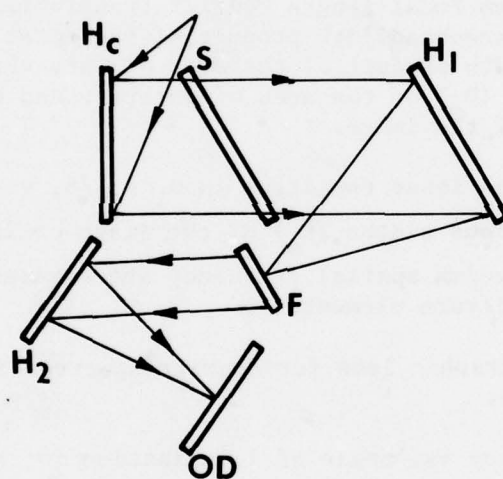
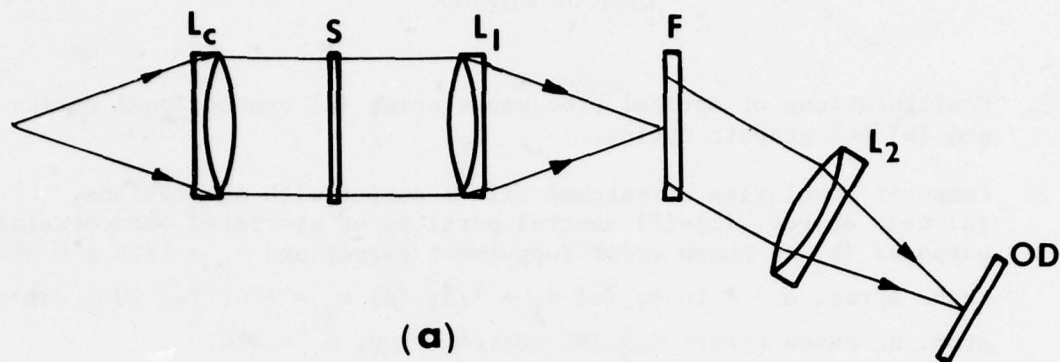


Figure 1. Configurations of optical processors using (a) conventional optics and (b) holographic optics.

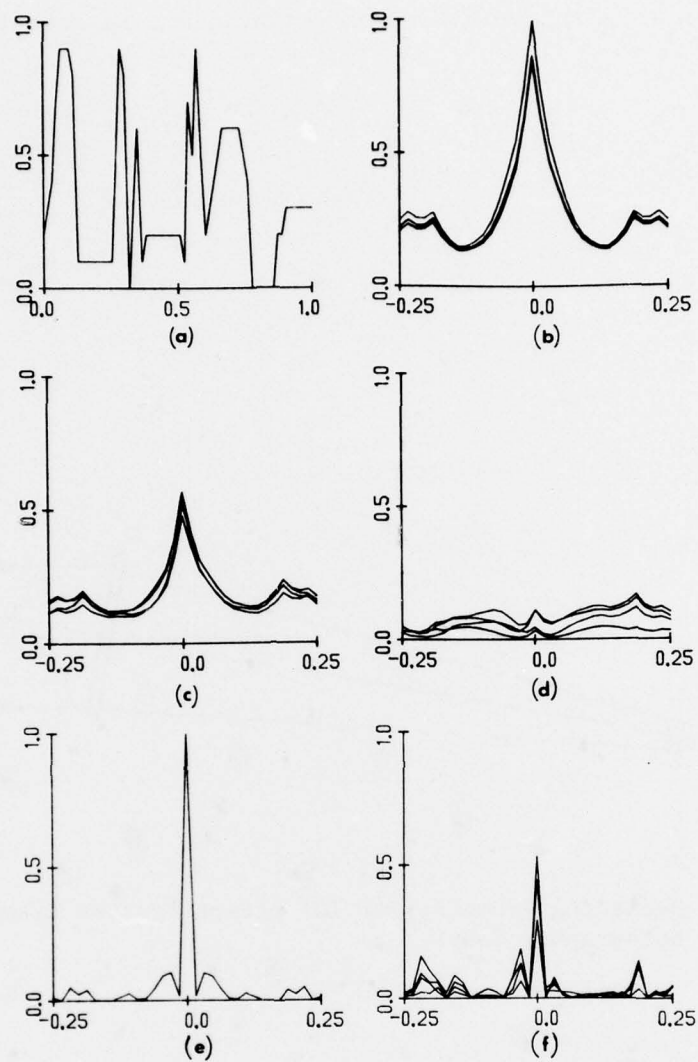


Figure 2. Computer simulation of matched filter output with aberrations. (a) Test object, (b)-(f) central portions of aberrated autocorrelation outputs: (b) no phase error (uppermost curve) and  $\sigma_1 = \lambda/16$   $n$ th order phase error,  $n = 1$  to  $4$ ; (c)  $\sigma_1 = \lambda/8$ ; (d)  $\sigma_1 = \lambda/4$ ; (e) 20% central stop, no phase error; (f) 20% central stop,  $\sigma_1 = \lambda/4$ .

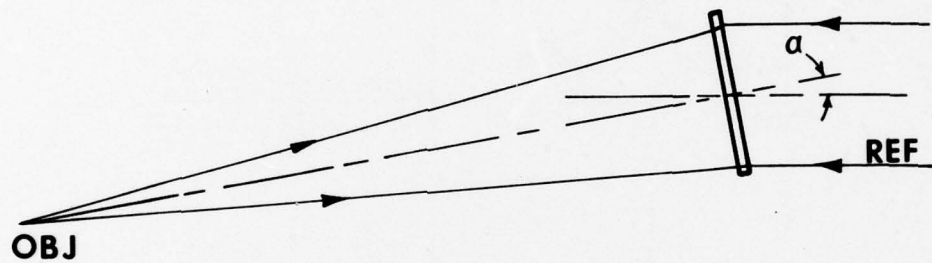


Figure 3. Recording geometry for 10° offset Fourier transforming holographic lens.

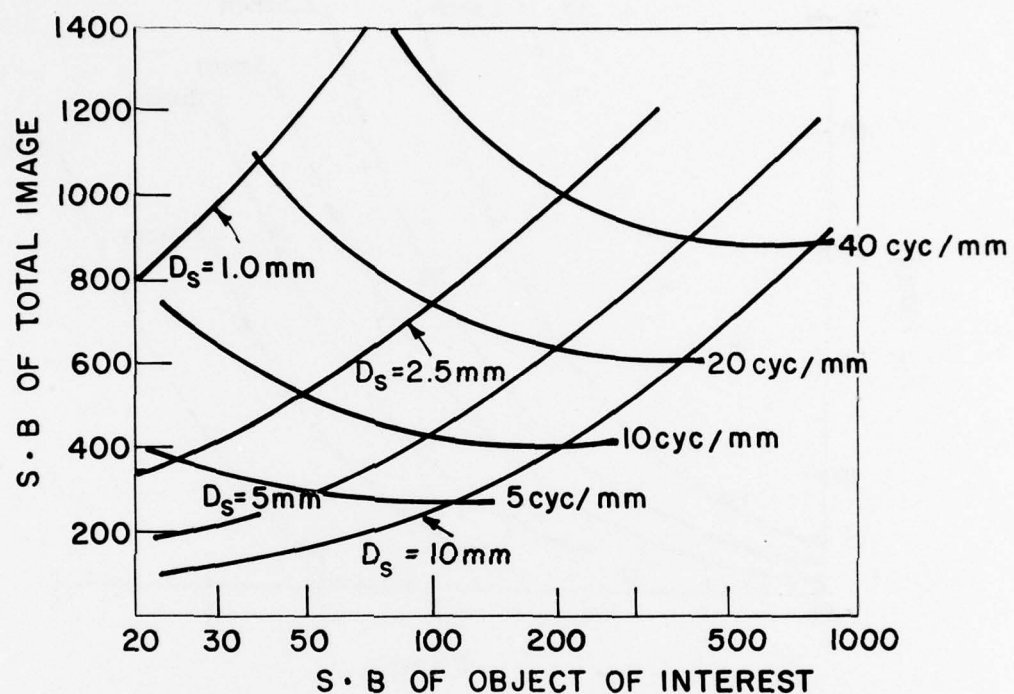


Figure 4. Performance of 100 mm focal length Fourier transforming holographic lens: the linear space-bandwidth product of the total image vs. the linear space-bandwidth product of the area of interest, for various values of the width ( $D_s$ ) of the area of interest and of the maximum spatial frequency of the image.



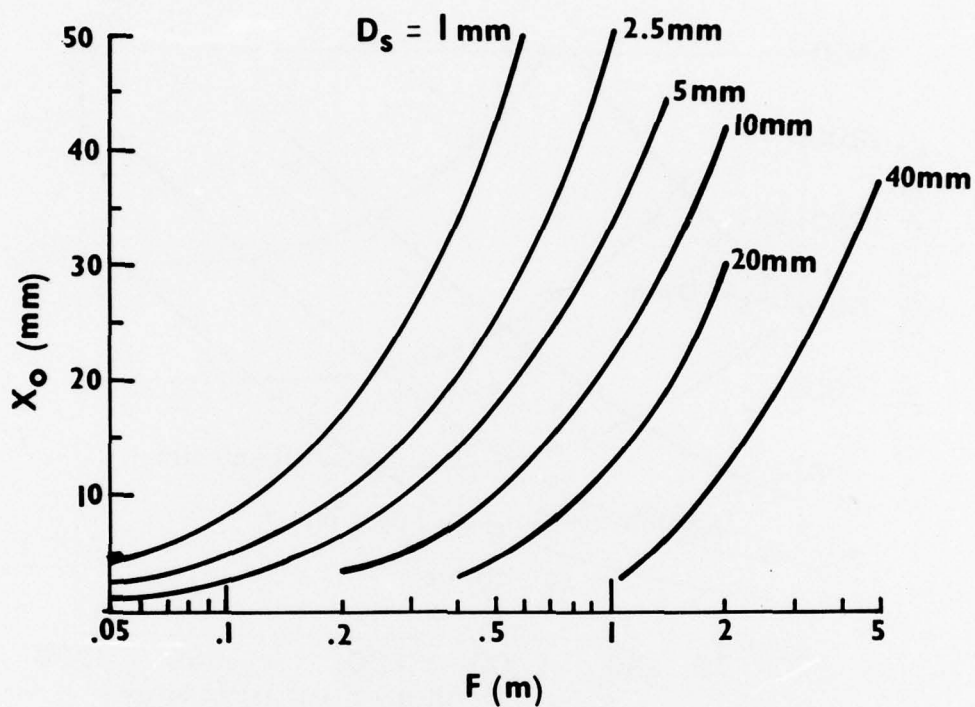


Figure 5. Translation  $x_o$  of the input resulting in  $\sigma_1 = \lambda/8$ , vs. focal length ( $F$ ), for various widths ( $D_s$ ) of the image of interest. A  $10^\circ$  offset and 40 cyc/mm spatial frequency are assumed, making 10 mm equivalent to 800 picture elements.

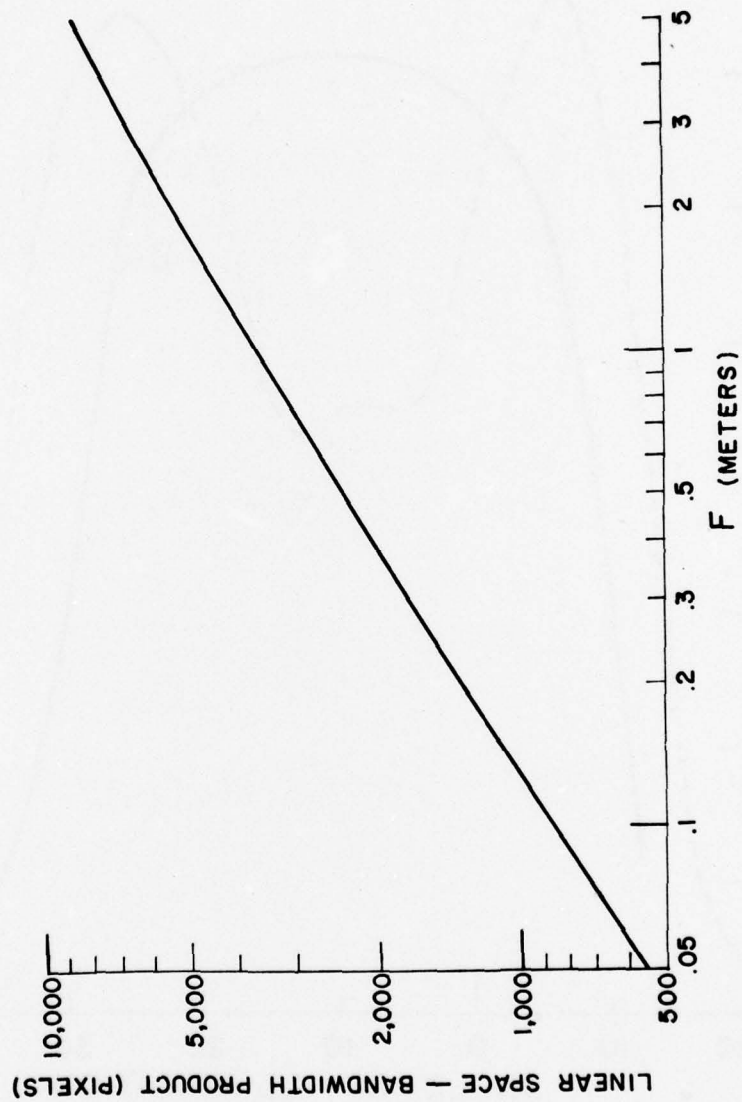


Figure 6. Performance of holographic lens for Fourier spectrum analysis, assuming  $\sigma \leq \lambda/8$  at 40 cyc/mm.

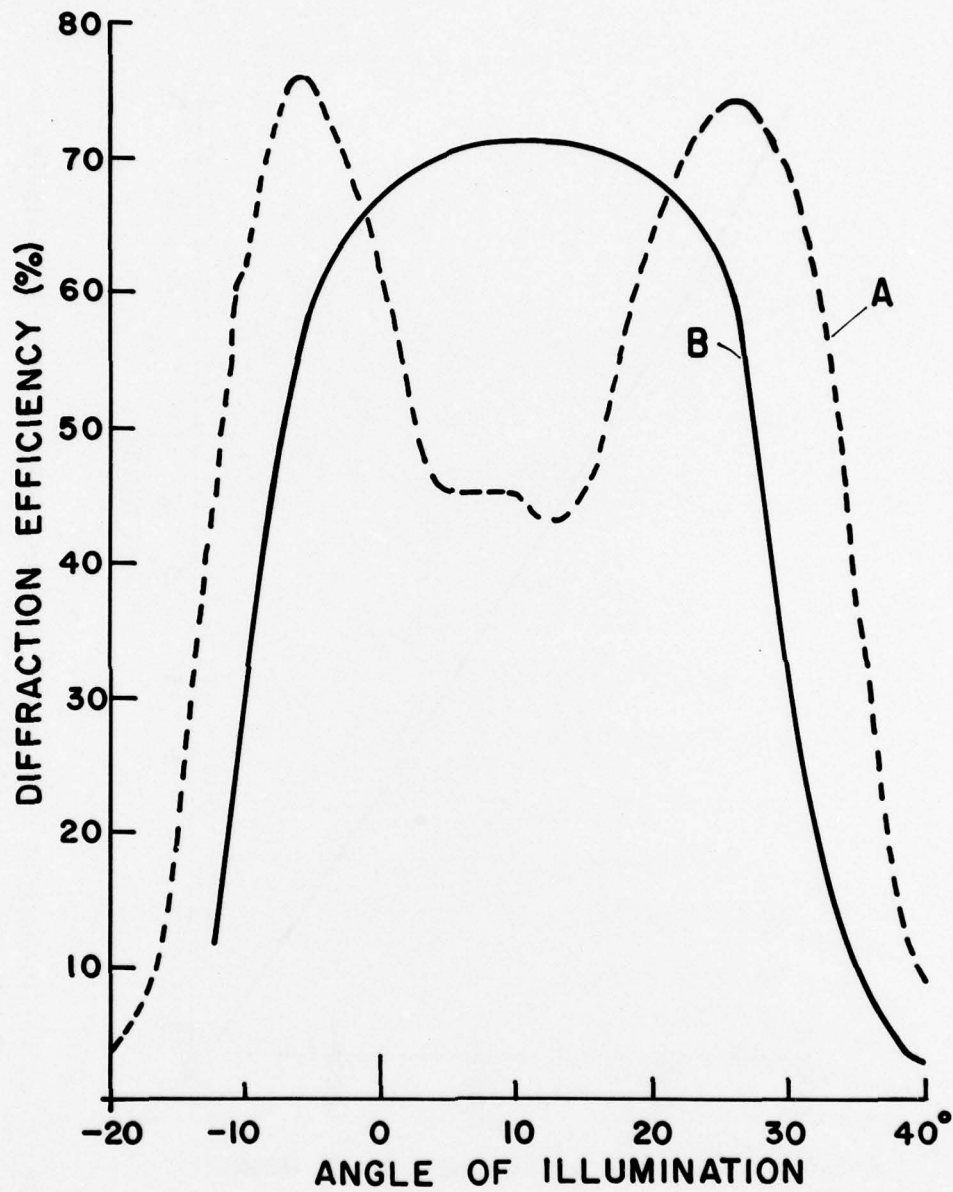


Figure 7. Diffraction efficiency vs. angle of illumination for holographic lenses A and B.

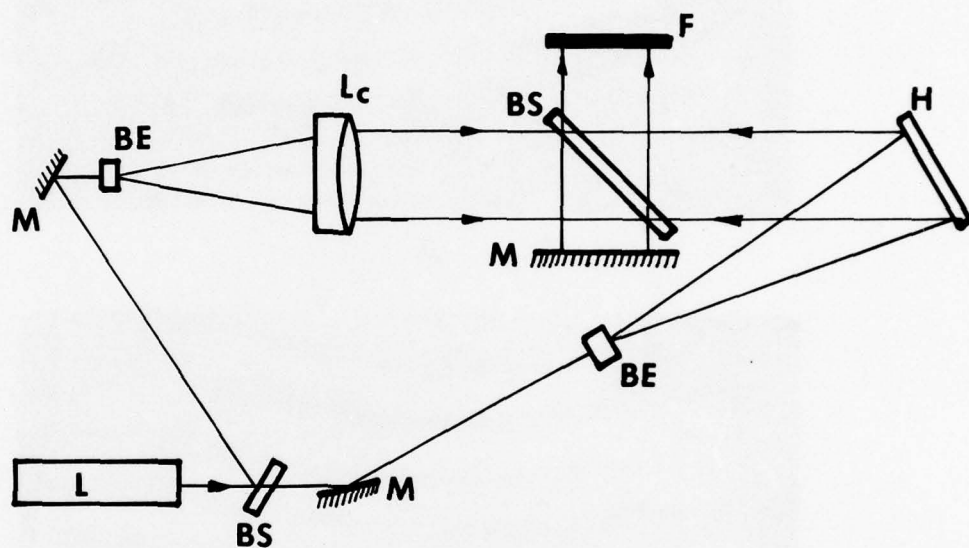
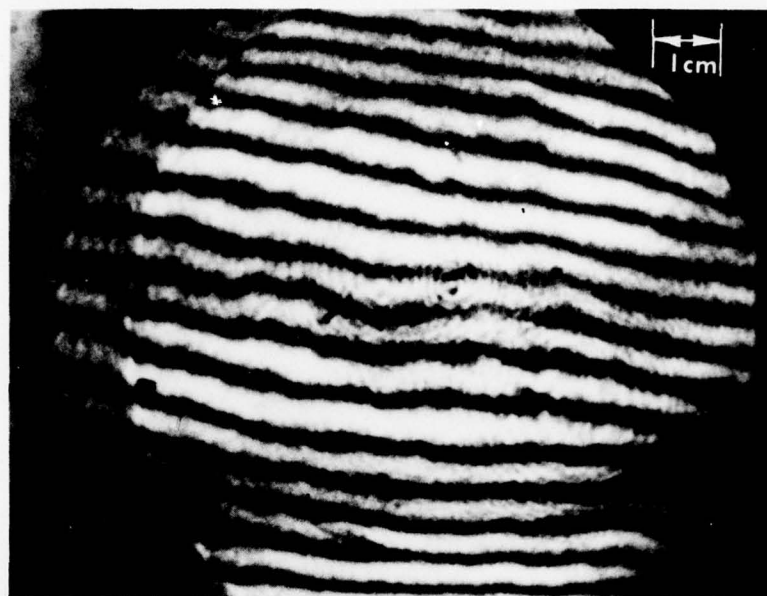


Figure 8. Interferometer for testing holographic lenses.





**A**



**B**

Figure 9. Interferograms of holographic lenses A and B.



Figure 10. Input image for correlation experiments.

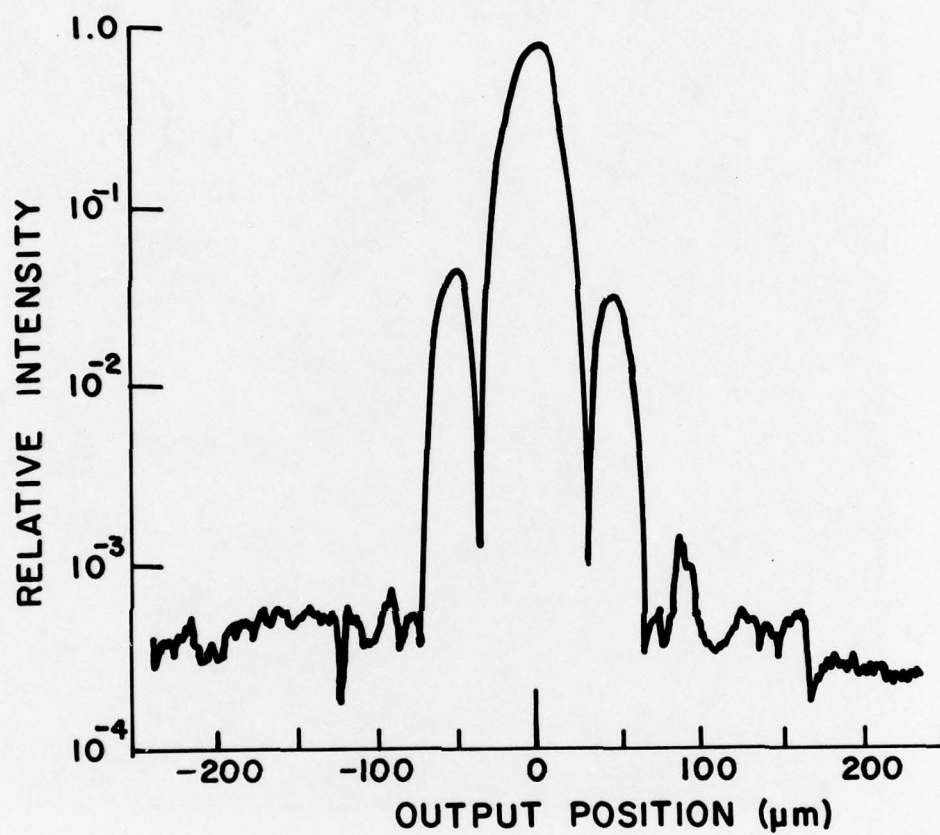


Figure 11. Scan through peak of output,  $x_o \approx 4$  mm.

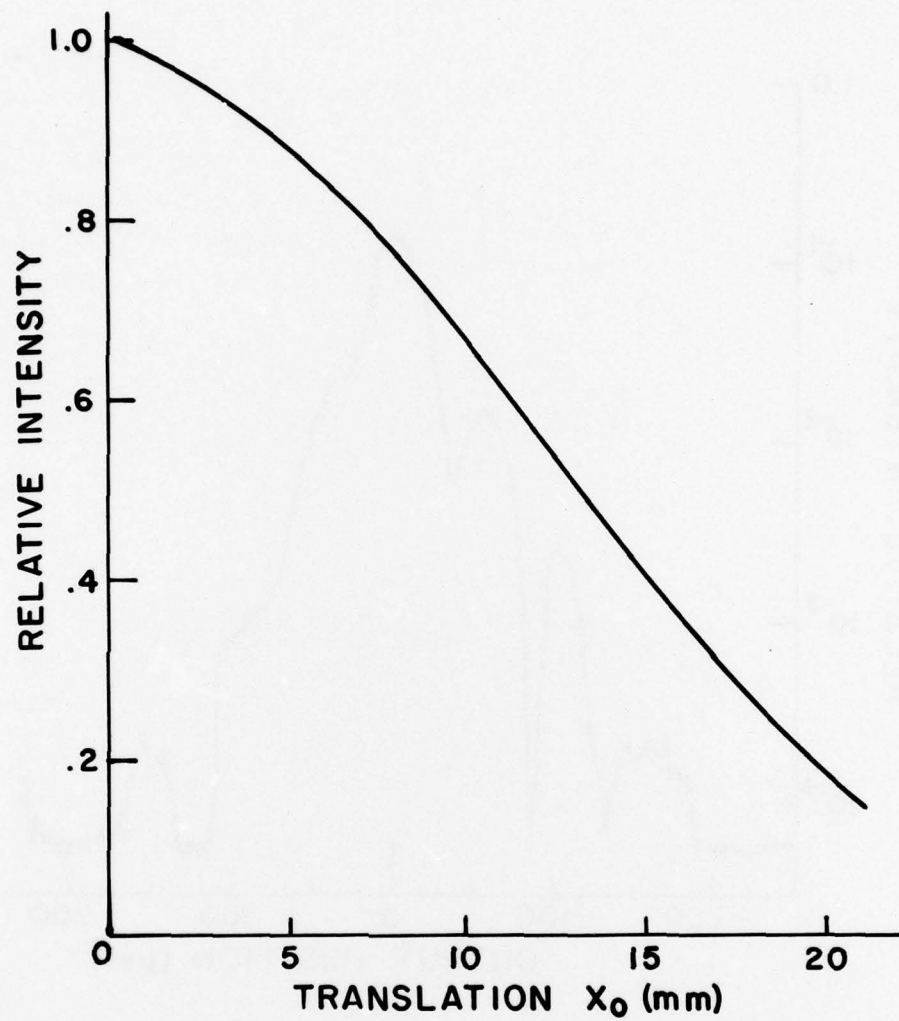


Figure 12. Intensity of output peak vs.  $x_0$ .



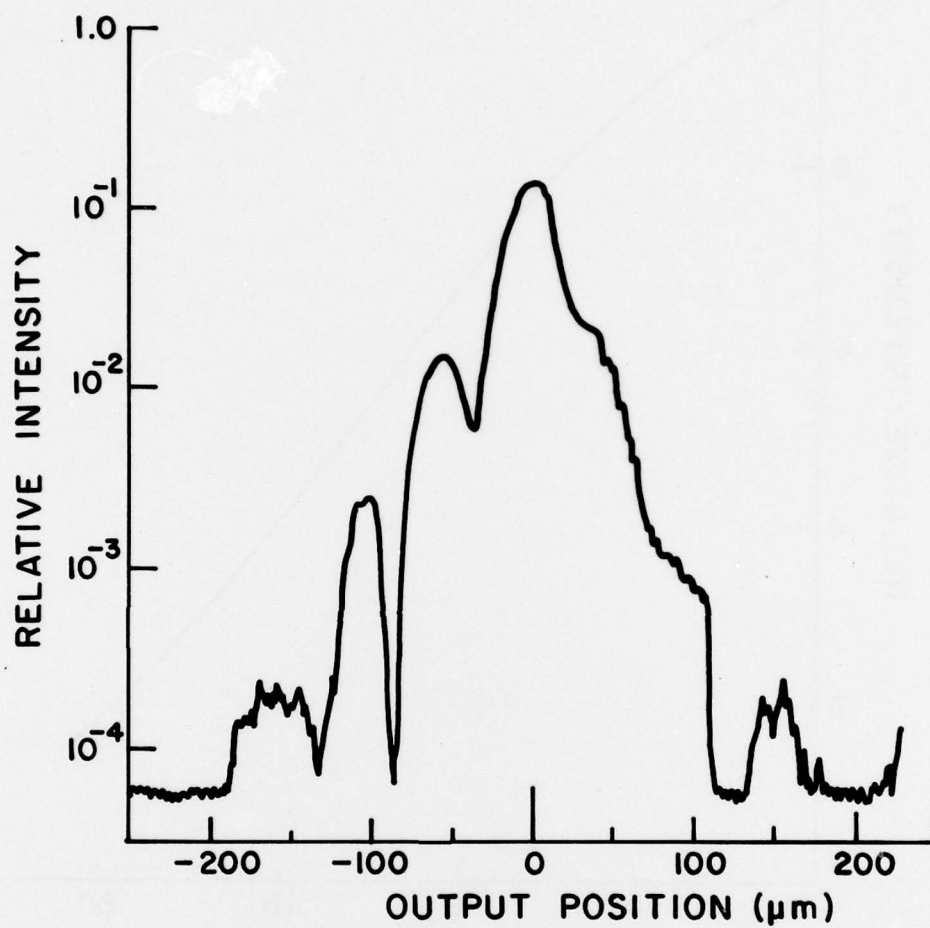


Figure 13. Scan through peak of output,  $x_o = 21$  mm.

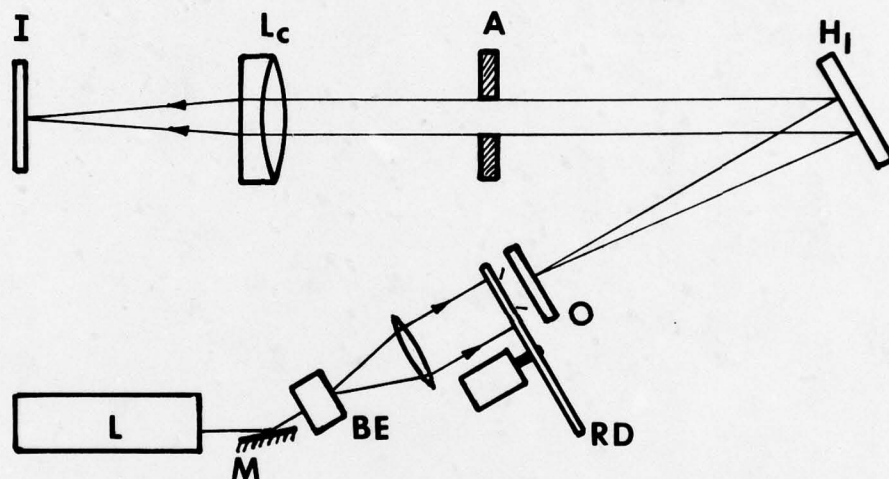
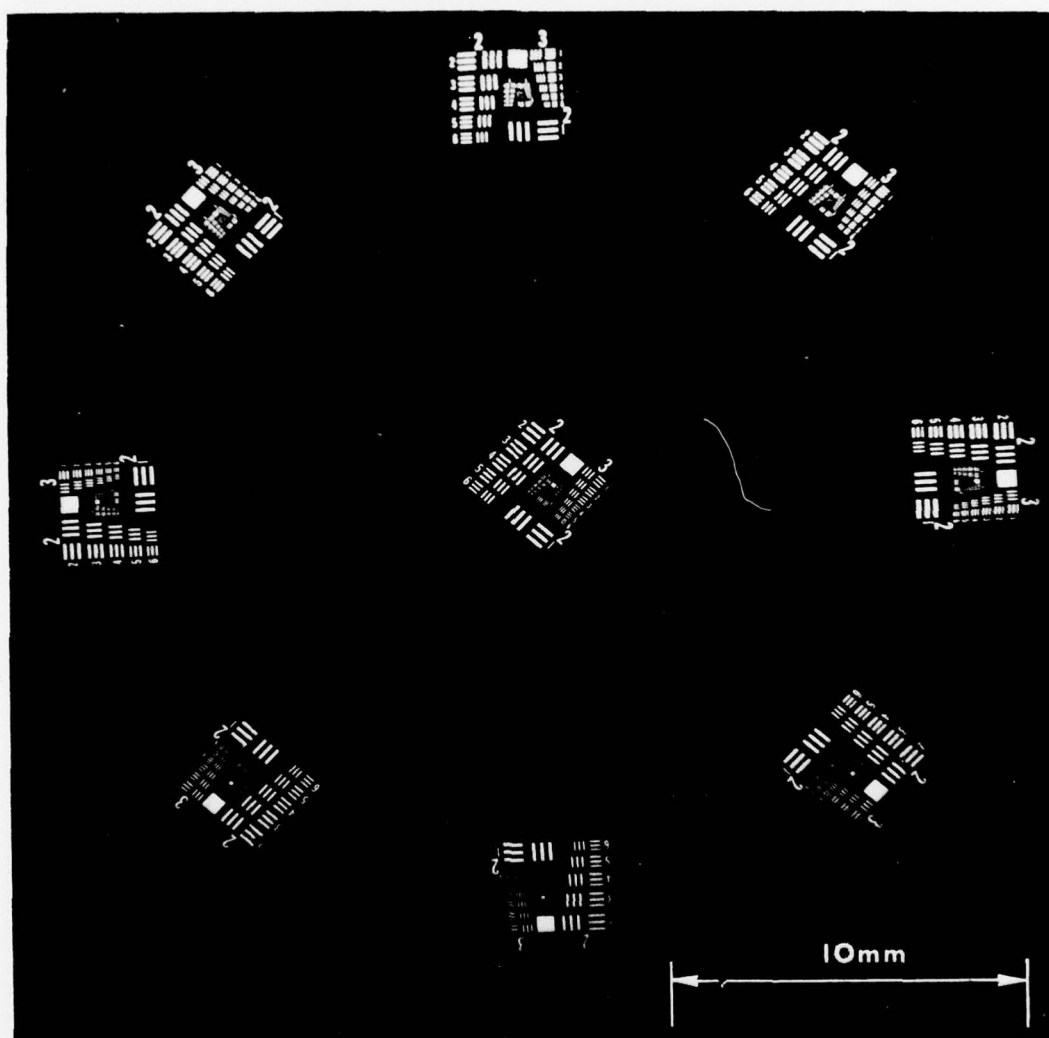
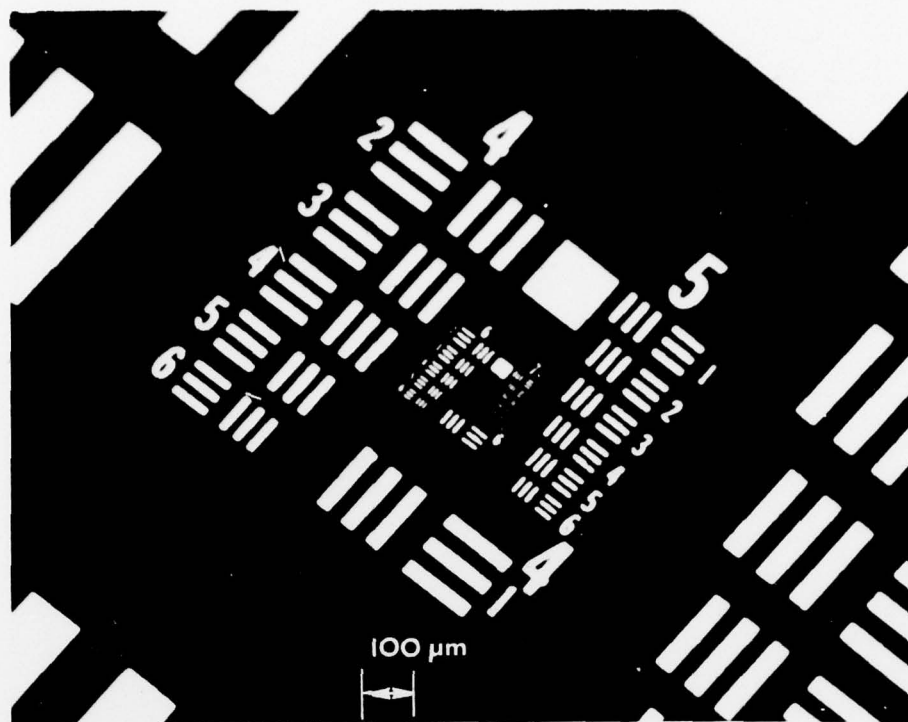


Figure 14. Imaging system using a holographic lens.

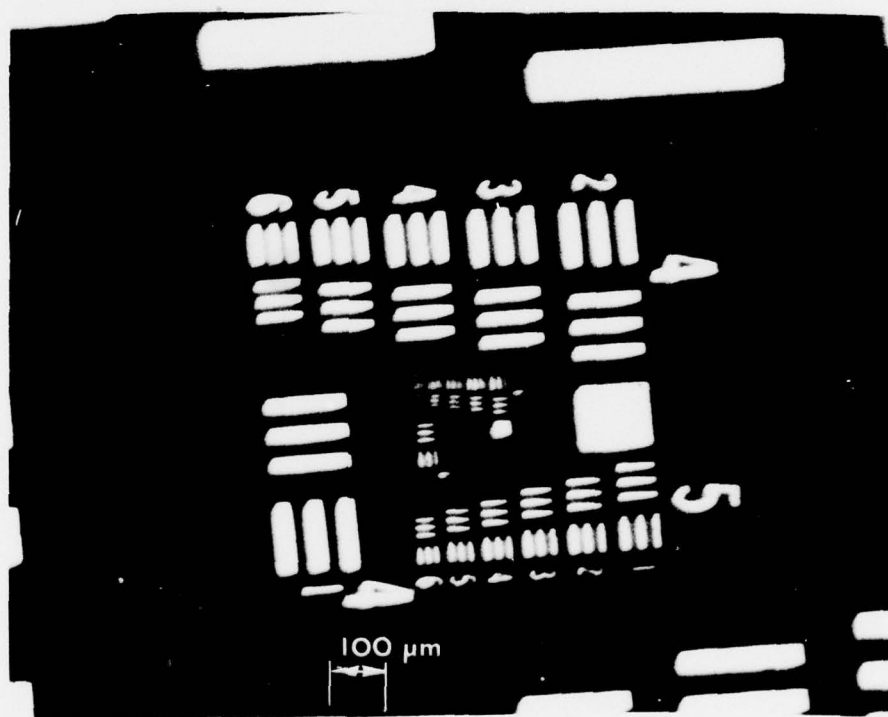


(a)

Figure 15. Output image. (a) Entire field-of-view.



(b)



(c)

Figure 15. Output image. (b) Magnified central area;  
(c) Magnified right side area.